Can 3D Multiparametric Ultrasound Imaging Predict Prostate Biopsy Outcome?

Ultrasound in Medicine & Biology 50 (2024) 1194–1202

Contents lists available at ScienceDirect

Ultrasound in Medicine & Biology

journal homepage: www.elsevier.com/locate/ultrasmedbio

Original Contribution

Can 3D Multiparametric Ultrasound Imaging Predict Prostate Biopsy Outcome?

Peiran Chen [a,*], Simona Turco [a], Yao Wang [b], Auke Jager [c], Gautier Daures [d], Hessel Wijkstra [a,c], Wim Zwart [d], Pintong Huang [b], Massimo Mischi [a]

[a] Department of Electrical Engineering, Eindhoven University of Technology, Eindhoven, Netherlands
[b] Department of Ultrasound in Medicine, The Second Affiliated Hospital of Zhejiang University, Hangzhou, China
[c] Department of Urology, Amsterdam University Medical Centers, Amsterdam, Netherlands
[d] Angiogenesis Analytics, JADS Venture Campus, Netherlands

ARTICLE INFO

Keywords:
Prostate cancer
Dynamic contrast-enhanced ultrasound
Ultrasound shear-wave elastography
Multiparametric ultrasound
Computer-assisted diagnosis

ABSTRACT

Objectives: To assess the value of 3D multiparametric ultrasound imaging, combining hemodynamic and tissue stiffness quantifications by machine learning, for the prediction of prostate biopsy outcomes.
Methods: After signing informed consent, 54 biopsy-naïve patients underwent a 3D dynamic contrast-enhanced ultrasound (DCE-US) recording, a multi-plane 2D shear-wave elastography (SWE) scan with manual sweeping from base to apex of the prostate, and received 12-core systematic biopsies (SBx). 3D maps of 18 hemodynamic parameters were extracted from the 3D DCE-US quantification and a 3D SWE elasticity map was reconstructed based on the multi-plane 2D SWE acquisitions. Subsequently, all the 3D maps were segmented and subdivided into 12 regions corresponding to the SBx locations. Per region, the set of 19 computed parameters was further extended by derivation of eight radiomic features per parameter. Based on this feature set, a multiparametric ultrasound approach was implemented using five different classifiers together with a sequential floating forward selection method and hyperparameter tuning. The classification accuracy with respect to the biopsy reference was assessed by a group-k-fold cross-validation procedure, and the performance was evaluated by the Area Under the Receiver Operating Characteristics Curve (AUC).
Results: Of the 54 patients, 20 were found with clinically significant prostate cancer (csPCa) based on SBx. The 18 hemodynamic parameters showed mean AUC values varying from 0.63 to 0.75, and SWE elasticity showed an AUC of 0.66. The multiparametric approach using radiomic features derived from hemodynamic parameters only produced an AUC of 0.81, while the combination of hemodynamic and tissue-stiffness quantifications yielded a significantly improved AUC of 0.85 for csPCa detection (p-value < 0.05) using the Gradient Boosting classifier.
Conclusions: Our results suggest 3D multiparametric ultrasound imaging combining hemodynamic and tissue-stiffness features to represent a promising diagnostic tool for biopsy outcome prediction, aiding in csPCa localization.

Introduction

Prostate cancer (PCa) is the most frequently occurring type of non-skin cancer and is the second-leading cause of cancer-related death in men [1].

In recent years, multiparametric MRI (mpMRI) has emerged as a key diagnostic tool and is increasingly being utilized for the detection of clinically significant PCa (csPCa) [2]. In the current European Association of Urology (EAU) guidelines on PCa, performing mpMRI before biopsy is strongly recommended for biopsy naïve patients [3]. When the MRI shows suspicious lesions, an MRI-targeted biopsy can be conducted for PCa detection. The MRI-targeted biopsy is typically performed by fusing the MRI images to the real-time B-mode ultrasound imaging, either by registration software or cognitively, and then guiding biopsies. Literature shows that MRI-targeted and transrectal ultrasound (TRUS)-guided biopsies do not differ in overall PCa detection, but that MRI-targeted biopsy has a higher rate of csPCa detection and a lower rate of insignificant PCa detection compared to TRUS-guided biopsy [4]. The ability of MRI to distinguish between indolent or insignificant PCa and csPCa is a key aspect. Notably, the lower sensitivity of MRI to insignificant over significant PCa may be beneficial in preventing overdiagnosis, as it may lead to overtreatment, thereby imposing an increased burden on patients [5]. Yet, mpMRI suffers from a poor reproducibility and specificity [6]. Moreover, limitations inherent to MRI-based diagnosis include high cost, limited availability, and impracticality for bedside use. In particular, MRI cannot provide real-time diagnosis and guidance

* Address correspondence to: Peiran Chen Department of Electrical Engineering, Eindhoven University of Technology, Eindhoven, Netherlands
E-mail address: p.chen1@tue.nl (P. Chen).

https://doi.org/10.1016/j.ultrasmedbio.2024.04.007
Received 28 November 2023; Revised 16 March 2024; Accepted 14 April 2024

for urologists, making the biopsy procedure complex and lengthy [7]. As reported in the latest EAU guidelines online [8], an MRI diagnostic pathway, in which patients with a positive MRI undergo only MRI-targeted biopsy, or patients with a negative MRI do not undergo biopsy, is appealing, as it could decrease the number of biopsy procedures. However, MRI findings must be interpreted in the light of the a priori risk of csPCa, and this diagnostic pathway has only been evaluated in patients whose risk of csPCa was judged high enough for biopsy referral based on standard clinical assessment [8].

As a cost-effective, widely available, practical, and real-time diagnostic tool for PCa, TRUS imaging comprises various imaging modalities such as B-mode, Doppler mode, dynamic contrast-enhanced ultrasound (DCE-US) and shear-wave elastography (SWE). Current B-mode and Doppler TRUS are not sufficiently accurate for TRUS-targeted biopsy and PCa detection due to the low sensitivity and specificity of B-mode and the limited sensitivity to microvascular flow of Doppler [9].

DCE-US imaging allows for the real-time visualization of blood flow and analysis of vascularization with the help of intravenously injected ultrasound contrast agents (UCAs). Tumor-driven angiogenesis is a recognized hallmark of cancer growth, which is characterized by a complex and irregular microvascular architecture [10]. Cancer-associated changes in the microvascular network can lead to tumor perfusion patterns that are distinguishable from those in normal tissue; this can be highlighted by DCE-US imaging. Hemodynamic quantifications based on DCE-US can thus be used for the characterization of cancer angiogenesis [11].

Typically, blood perfusion parameters are extracted from DCE-US time-intensity curves (TICs) to characterize malignant tissues in the prostate [12–15]. TICs can be obtained at each pixel by collecting the pixel intensity variations over the DCE-US loops, reflecting the temporal evolution of the UCA concentration. TIC linearization is usually performed prior to the analysis to compensate for the nonlinearities introduced by the scanner, such as the typical log-compression [16,17].

More recently, contrast-ultrasound dispersion imaging (CUDI) has been developed to quantify DCE-US acquisitions by modeling the spatio-temporal evolution of the UCA concentration as a convective-dispersion process. This allows for the extraction of blood perfusion and contrast dispersion parameters. As reported in [18–22], dispersion parameters reflect more effectively than perfusion parameters those changes in the underlying microvascular architecture that are associated with cancer angiogenesis. The obtained CUDI parameters can be further extended by derivation of radiomic features; their combination have indeed shown promising results for the localization of PCa [23–25]. The recent advances in 3D DCE-US imaging provide the possibility to acquire the UCA perfusion across the full prostate gland in one examination using a single bolus injection. Based on this, 3D CUDI has been developed, enabling the hemodynamic quantifications in the whole prostate [25–27]. Moreover, 3D imaging allows for a better definition of the boundary conditions for directly modeling the 3D behavior of the UCA spreading through the prostate as a convective-dispersion process [28].

In addition to cancer angiogenesis, tissue stiffness has also proven to be an effective biomarker for assessing PCa. In the prostate, tissue stroma reacts to the invasion of cancer cells by eliciting a wound repair mechanism. This results in elevated collagen deposition in tumor regions, leading to increased stiffness compared to normal tissues [29,30]. Several studies have shown the clinical value of ultrasound SWE for PCa detection by quantifying tissue stiffness [31–34]. Currently, TRUS-based SWE scanning is still limited to 2D acquisitions for most ultrasound scanners, although a novel application of 3D SWE in the detection of csPCa was investigated [35].

As different imaging modalities may contribute to PCa diagnosis complementally [36], several studies have reported on multiparametric ultrasound imaging, aiming at improving the diagnosis performance by combining B-mode imaging and power/color Doppler imaging [37], by combining B-mode imaging, color Doppler, real-time elastography, and enhancement patterns extracted from DCE-US acquisitions [38], by combining B-mode imaging, acoustic radiation force impulse imaging and shear wave elasticity imaging based on elasticity, as well as quantitative ultrasound imaging based on the spectral content of the backscattered ultrasound signals [39], or by combining B-mode imaging, SWE elasticity, and hemodynamic quantifications of DCE-US acquisitions [24]. These studies have shown that multiparametric ultrasound outperforms a single imaging modality in localizing PCa. However, these studies are limited to 2D acquisitions and lack quantitative DCE-US analysis.

In this work, a 3D multiparametric ultrasound imaging approach, combining hemodynamic quantifications represented by CUDI parameters with tissue-stiffness (elasticity map) measured by SWE, was implemented and evaluated for csPCa classification. To overcome the unavailability of 3D SWE, which hampers the fusion of SWE and 3D DCE-US, here we implement a 3D reconstruction of SWE elasticity maps based on multi-plane 2D acquisitions on the same prostate. Individual parameters along with their multiparametric combination by machine learning and radiomics, were evaluated for their ability to detect the presence of csPCa in regions corresponding to the systematic biopsy (SBx) samples, using the biopsy outcomes as a reference.

Materials and methods

Data acquisition

At the Second Affiliated Hospital of Zhejiang University (Hangzhou, China), 54 biopsy-naïve patients underwent a multi-plane 2D SWE scan with manual sweeping from base to apex of the prostate using an Aixplorer scanner (SuperSonic Imagine, France) equipped with a SE12-3 endocavity probe. During the multi-plane 2D SWE scan, an experienced ultrasound examiner first swept the probe from the base to the apex of the prostate, evaluating the prostate size; then, the ultrasound examiner started acquiring 2D SWE images with minimal compression from base to apex in an equal-angle sampling fashion. A 10-s stabilization period was taken after the acquisition of each plane. In the end, 10 planes of 2D SWE images were obtained for each prostate, except for few large prostate glands. Five to ten minutes were usually taken for a whole SWE scan. For each scan, the range of shear wave elastic modulus was set to 0–70 kPa, which enabled distinguishing between normal and malignant tissues as the typical elastic modulus for normal tissue is about 30 kPa. Subsequently, the same patients underwent a 2-min 3D DCE-US recording using a LOGIQ E9 scanner (GE HealthCare, USA) equipped with an RIC5-9-D transrectal probe following the intravenous administration of a 2.4-mL SonoVue® (Bracco, Italy) UCA bolus. For the 3D DCE-US acquisitions, the image quality "BQ" was set to "low," maximizing the temporal resolution to about 0.3 Hz. A low mechanical index of 0.09 was adopted by setting the output power (AO%) to "10," to avoid disruption of UCA microbubbles. The dynamic range and gain were set such that the measured TICs had no saturation. After ultrasound scanning, the same patients received a 12-core transrectal SBx procedure under TRUS guidance by the same ultrasound examiner using a Philips iU22 ultrasound system (Philips Healthcare, Bothell, WA, USA) equipped with a 2D transrectal probe (C9-5ec) in a dedicated operation room. The total procedure took about an hour including preparations, DCE-US imaging, SWE imaging, and the following biopsy, and all the patients were conscious during this period. The SBx cores were then histopathologically classified by a pathologist with 10 y of experience as benign, clinically insignificant PCa with Gleason score $3+3=6$, or csPCa with Gleason score $> 3+3$. In total, 639 biopsies were performed (Note that one or more biopsies were missing from three patients, for a total of nine. Of the 639 biopsies, the Gleason scores of six biopsies were not given as two Gleason patterns to be added together to obtain the Gleason score. Four biopsies were given the Gleason score of 6. One biopsy was given a Gleason score of 8. And one biopsy was without a score. These biopsies are not included in Table 1). In this study, the inclusion criteria were age > 18 y and the patients had elevated prostate-specific antigen (PSA) levels above 4 ng/mL. The procedure was approved by the local

Table 1
Characteristics of the patient group

Characteristics [unit]	Value
Number of patients [-]	54
Benign	34
Clinically significant cancer	20
Age, median (IQR) [years]	68 (65–73)
PSA, median (IQR) [ng/mL]	7.6 (5.4–14.4)
Biopsy results [-]	
Benign	473 (74.0%)
Gleason score	
3 + 3 = 6	45 (7.0%)
3 + 4 = 7	45 (7.0%)
4 + 3 = 7	21 (3.3%)
4 + 4 = 8	16 (2.5%)
> 4 + 4 = 8	33 (5.2%)

IQR, interquartile range; PSA, prostate-specific antigen.

ethics committee (Institutional Review Board from The Second Affiliated Hospital of Zhejiang University, No. IR2019001226) and all patients signed informed consent. The patient and tumor characteristics are summarized in Table 1.

Ultrasound data processing and multiparametric ultrasound imaging

Figure 1 presents an overview of the proposed multiparametric ultrasound imaging for PCa localization at the biopsy-region level. The details are given in the following sections.

DCE-US: Pre-processing

The DCE-US data were obtained by using the RIC5-9-D intracavital probe consisting of a wobbling curved array, resulting in the speckles in the ultrasound images being highly anisotropic and depth-dependent. To avoid the anisotropy and depth-dependency impacting on the TIC analysis, we performed a speckle size regularization to achieve an isotropic spatial resolution of 0.8 mm in all directions (axial, lateral, and elevational) [26]. Next, the data were spatially downsampled by a factor of 3, and cropped according to the prostate boundaries that were delineated in consensus by two urologists with 5 y of experience. To mitigate residual tissue clutter and noise signals in the spatiotemporal domain, as needed by part of the CUDI analysis, singular value decomposition (SVD) was applied to filter the DCE-US data [40].

DCE-US: CUDI analysis

In the classical work of Taylor, the transport of an indicator along an infinitely-long tube is described as a combination of convection along the flow direction, producing a parabolic flow profile in the case of laminar flow, and molecular diffusion in the radial direction due to concentration gradient [41]. These phenomena combined contribute to the so-called apparent diffusion [20,21,42,43]. In the case of flow through a distributed network, diffusion is dominated by the distribution of transit times determined by the multipath trajectories within the network, and it can more appropriately be referred to as dispersion [44]. The transport dynamics of UCAs in the prostate microvascular networks can thus be interpreted as a convective dispersion process. This builds the basis of CUDI techniques. In CUDI, the evolution of the UCA concentration in the prostate is modeled by the mono-dimensional convective-dispersion equation:

$$\partial_t C(z,t) = D\partial_t^2 C(z,t) - v\partial_z C(z,t), \tag{1}$$

where $C(z,t)$ is the UCA concentration at position z and time t, defining the TIC at position z; D is the dispersion coefficient; v is the convective velocity. D is assumed to be locally constant.

A modified local density random walk (mLDRW) model, as an analytical solution of the convective-dispersion equation [18], can be fitted to individual TICs measured at each voxel of the DCE-US data. The model is described as

$$C(t) = \alpha\sqrt{\frac{\kappa}{2\pi(t-t_0)}}\exp\left(-\frac{\kappa(t-t_0-\mu)^2}{2(t-t_0)}\right), \tag{2}$$

where the scale factor α, representing the temporal integral of $C(t)$, is related to the UCA dose and blood flow; μ is the mean transit time, representing the average time that the UCA bolus takes to travel from the injection to the detection site; t_0 is the theoretical bolus injection time and κ is the local dispersion-related parameter. A mean squared error minimization procedure was performed when fitting TICs by the model, enabling the estimation of α, μ, and κ [25]. This method is named *model-fit analysis*. Moreover, typical *perfusion parameters* can also be extracted from the fitted TICs, including wash-in-time (*WIT*), wash-in-rate (*WIR*), and appearance time (*AT*) of the UCA bolus, as well as peak intensity (*PI*) of the curves [12–15].

The multipath trajectories of UCAs through a microvascular network determine the dispersion kinetics of UCAs [44]. In addition, by a finite-difference simulation of the mono-dimensional convective-dispersion equation, different values of D result in changes in TIC shapes [21]. Thus, in a local region, the shape similarity between TICs can reflect the local degree of dispersion, and further reflect the underlying changes in the microvascular architecture. The *spatiotemporal similarity analysis* allows the assessment of the similarity between neighboring TICs in a shell-shaped kernel by calculating similarity measures, such as the spectral coherence (ρ), temporal similarity (r) and mutual information (*MI*) [19–21,45]. Taking into account the spatial resolution of the imaging system and the scale at which angiogenesis occurs, the inner and outer kernel radius were set to 1.0 and 2.5 mm, respectively.

Instead of modeling the individual TICs, the microvascular network can be considered as a dynamic dilution system, whose impulse response

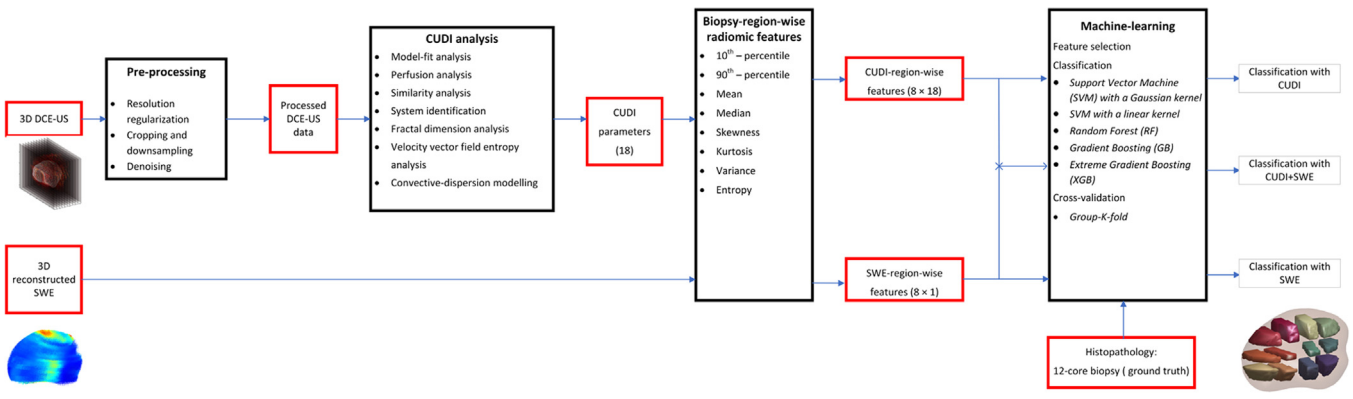

Figure 1. An overview of the proposed multiparametric ultrasound imaging for PCa localization at the biopsy-region level.

can be locally identified by input-output analysis of TICs measured from two voxels with a certain distance L. As the UCA flow through the microvascular network is governed by eqn (1), its Green's function represents spatiotemporally the impulse response of the system [22]:

$$g\left(t\middle|L,\ v,D\right) = \frac{H(t)}{\sqrt{4\pi Dt}}\exp\left(-\frac{(L-vt)^2}{4Dt}\right), \quad (3)$$

where $H(t)$ is the Heaviside step function. Based on that, the input-output analysis can be performed by minimizing the sum of the squared difference between the output TIC and the convolution of the input TIC with $g(t|L,\ v,D)$, providing local estimates of v and D. A measure of the relative contribution between the dispersion and convection processes, the Péclet number (*Pe*), can also be derived based on the estimated v and D. For the 3D DCE-US acquisitions, the *system-identification* method is implemented in a shell-shaped kernel that moves over the whole prostate region. The kernel has an inner and outer radius of 1 and 2 mm, respectively, in which the TIC extracted from the central voxel is used as the input TIC and the output TIC is extracted from the shell. Prior to the system identification, cross-correlation analysis is performed for selection of those TICs within the kernel that satisfy causality [22].

By directly *modelling the 3D behavior of the UCA bolus spreading through the whole prostate as a convective-dispersion process*, we can solve eqn (1) as a linear system in a 3D kernel to estimate the convective velocity and dispersion. The 3D spherical kernel has a diameter of 7 voxels, within which the local least-squares problem is solved in an L_2-regularization fashion [27]. Here, the obtained v and D are the convective velocity vector field and the convective dispersion tensor, respectively. Subsequently, they are quantified by the magnitude of velocity using $\sqrt{v_x^2+v_y^2+v_z^2}$, and by the convective dispersion coefficient using $\left|\frac{D_{xx}+D_{yy}+D_{zz}}{3}\right|$, respectively, where v_x, v_y, and v_z are the velocity vector components in space and D_{xx}, D_{yy}, and D_{zz} are the diagonal elements of the convective dispersion tensor. Based on the obtained convective velocity vector fields, the *entropy (Entropy)* and *conditional entropy (CEntropy)* of the vector field are also calculated using the 3D extension of the method described in [46]. The entropy analysis aims at providing a measure of vascular heterogeneity.

Moreover, a geometrical measure of the vascular architecture is realized by the *fractal dimension analysis*, which builds on the relation between the fractal dimension (*FD*) and the relative dispersion of local blood flow [25,47].

As such, 3D parametric maps of the 18 resulting CUDI parameters that quantify the prostate hemodynamics can be generated.

3D reconstruction of SWE

Ultrasound SWE elasticity offers a quantitative way to characterize tissue stiffness, enabling us to discriminate between benign and malignant prostate tissue [31–34]. To combine the SWE elasticity and the CUDI parameters introduced above, a 3D SWE elasticity map was reconstructed based on multi-plane 2D SWE acquisitions on the same prostate. During the acquisition, regular sampling of the SWE imaging planes at equal-angle intervals from the base to the apex of the prostate was performed. For each prostate, the longitudinal-plane ultrasound B-mode image was employed to determine the angle of the base and apex image planes, and the other angles were calculated subsequently. From these angles, the 3D coordinates of each SWE plane were calculated and the elasticity values in the 2D planes were assigned to their corresponding positions in the 3D space. The assigned elasticity values were then interpolated between planes using the nearest neighbor method.

Biopsy-region-wise radiomic features

First, the prostate model in the 3D CUDI parametric maps and SWE elasticity map was segmented based on the delineated prostate contour. Second, each prostate model was subdivided into 12 regions corresponding to SBx locations. The regions extended approximately 22 mm in the anterior direction, which is the length of the biopsy needle [25]. This length ensured that the regions were located in the peripheral zone. Moreover, the regions were constructed under slight lateral angles and with an inter-region interval [25], according to the SBx template as described in [48]. Third, in each region, the radiomic features of each CUDI parameter and SWE elasticity were derived, comprising the median, 10th-percentile, 90th-percentile, mean, skewness, kurtosis, variance, and entropy [49].

Finally, for each prostate, 152 region-wise radiomic features (12 SBx regions, 18 CUDI parameters and 1 SWE elasticity, 8 radiomic features per parameter per region) were computed and used for multiparametric ultrasound imaging.

Machine-learning

A machine learning framework was implemented to process the biopsy-region-wise radiomic features, realizing multiparametric ultrasound imaging for PCa prediction. Five classifiers were used as model candidates: Support Vector Machine (SVM) with a Gaussian kernel, SVM with a linear kernel (LSVM), Random Forest (RF), Gradient Boosting (GB) and extreme Gradient Boosting (XGB). Firstly, the hyperparameters of the classifiers were optimized by a grid search based on all the 152 radiomic features. This aims at providing a preliminary optimal set of hyperparameters. Secondly, given the classifiers and their respective hyperparameters, feature selection was performed using a sequential floating forward selection (SFFS) [50]. At each step forward, the SFFS method evaluates the performance and adds or removes features when this improves the performance. For each classifier, the feature selection procedure was run separately, setting the maximum number of selected features to 18. As such, the best subset of biopsy-region-wise radiomic features was found for each classifier. Thirdly, Bayesian-optimization-based hyperparameter tuning was applied to these classifiers, aiming not only at finding the final optimal hyperparameters per classifier but also at determining the classifier holding the best csPCa classification performance [51]. At each of the three steps above, biopsy-region-level group-k-fold cross-validation was employed to evaluate the performance. The 54 patients were divided into 9 folds using the group-k-fold method, ensuring that biopsies from the same patients were not in two different folds (grouping by patient). At each rotation of the grouped cross-validation procedure, region-wise radiomic features from 6 patients were used for validation (1-fold), while data from patients in the remaining 8 folds were used as the training set. The SBx outcomes were used as the reference. In the cross-validation procedure, the Area Under the Receiver Operating Characteristics Curve (AUC) was used to evaluate the classification performance. The mean and standard deviation (std) of the AUC over the folds were also calculated. The machine-learning procedure was implemented on a Linux server with the AMD Ryzen™ 9 3950X 16-Core Processor, which took about 2 h for training and cross-validation steps.

Results

Classification performance with individual features

An example of all the 18 3D CUDI parametric maps and a 3D SWE elasticity map in the same csPCa patient is depicted in Figure 2. To evaluate the classification performance of multiparametric ultrasound imaging, Table 2 demonstrates the diagnostic potential of individual CUDI parameters and SWE elasticity to distinguish between benign tissue and csPCa.

Classification performance with the multiparametric approach

Figure 3 is the feature selection ranking plot obtained when implementing the multiparametric approach. In this plot, for each feature, the number of classifiers selecting it (regardless of AUC) as a member of their best feature subset is expressed by the height as well as the color

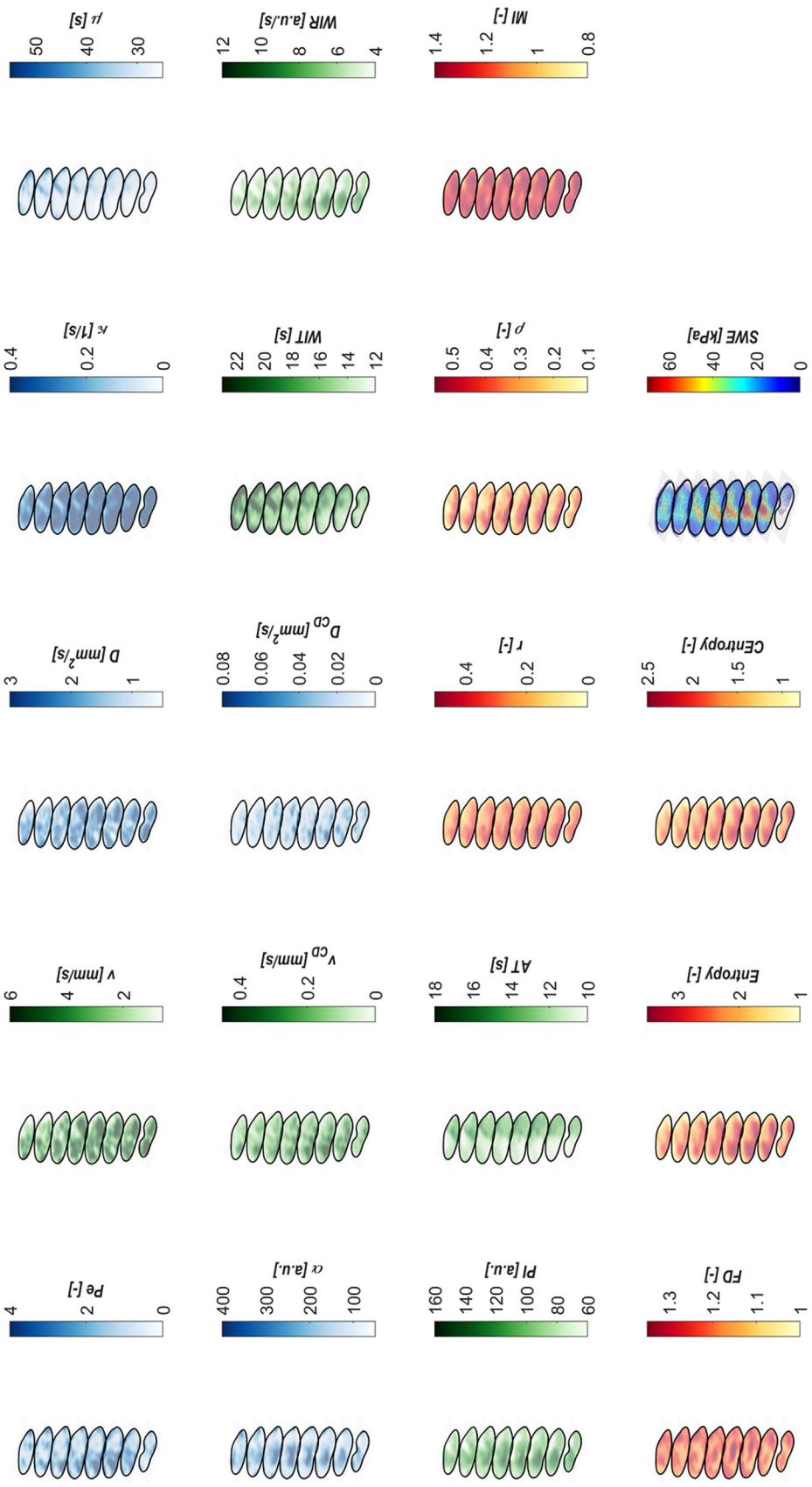

Figure 2. Example of all 18 3D CUDI parametric maps and a 3D SWE elasticity map in the same PCa patient. The SBx outcomes reveal that csPCa happens in the left part of the prostate. The SBx results are shown in Figure 4.

Table 2
Classification performance of individual parameters

Feature	AUC (mean ± std)
Model-fit analysis	
κ	0.70 ± 0.12
μ	0.72 ± 0.14
α	0.68 ± 0.08
Typical perfusion analysis	
WIT	0.72 ± 0.14
WIR	0.73 ± 0.11
PI	0.71 ± 0.10
AT	0.73 ± 0.13
Spatiotemporal similarity analysis	
r	0.70 ± 0.13
ρ	0.74 ± 0.10
MI	0.75 ± 0.11
System identification	
v	0.69 ± 0.07
D	0.70 ± 0.10
Pe	0.63 ± 0.10
3D convective-dispersion modelling	
v_{CD}	0.74 ± 0.08
D_{CD}	0.72 ± 0.09
Entropy analysis	
Entropy	0.71 ± 0.12
CEntropy	0.69 ± 0.06
Fractal dimension analysis	
FD	0.66 ± 0.07
Ultrasound shear-wave elastography	
SWE	0.66 ± 0.12

shade of the bar. The maximum number of selections is five due to total number of classifiers. In the end, the number of features selected by the classifiers, SVM, LSVM, RF, XGB, and GB, is 10, 7, 13, 14, and 11, respectively. *FD* and SWE elasticity are selected by all the classifiers. Among the five classifiers, the GB classifier gave the best performance for csPCa classification with an AUC value of 0.85 using the following features: "median of r," "90th-percentile of μ," "90th-percentile of *FD*," "entropy of *Pe*," "entropy of v_{CD}," "entropy of κ," "entropy of *CEntropy*," "variance of v," "skewness of ρ," "skewness of *WIT*," "skewness of *FD*," "kurtosis of *CEntropy*" and "90th-percentile of *SWE*." As a comparison, we also computed the performance when using only the CUDI parameters by the proposed multiparametric procedure. This resulted in an AUC of 0.81, with GB remaining the best classifier as well. It is higher than all the AUC values using individual CUDI parameters, but significantly lower than the AUC value obtained by the proposed multiparametric procedure using the combination of CUDI and SWE with a p-value of 0.002 (p-value < 0.05), as shown in Table 3. The significance of the difference (p-value) was assessed by the single-tailed Wilcoxon signed-rank test with the 9-fold AUC values obtained in the cross-validation procedure as the two groups of input. The employment of the Wilcoxon signed-rank test was due to the non-normality of the two groups of the input that was assessed by the Shapiro-Wilk test [52] as well as due to the two groups of the input being paired.

Table 3
Classification performance of the multiparametric approach

Multiparametric approach	AUC (mean ± std)
CUDI	0.81 ± 0.12
CUDI and SWE	0.85 ± 0.11

Figure 4 shows an example of the SBx outcomes and the csPCa prediction results obtained by the proposed multiparametric approach combining CUDI parameters and SWE elasticity. Indeed, most regions predicted to have cancer correspond to the regions with histopathologically confirmed csPCa.

Discussion

Considering the multi-focal nature of PCa and the low detection rate of csPCa by SBx [53–55], reliable techniques that can guide targeted biopsies are essential to identify cancer foci.

mpMRI scanning and subsequent mpMRI-targeted biopsy have been shown to produce accurate csPCa detection, and this procedure is strongly recommended by the European Association of Urology [3]. However, as MRI cannot provide urologists with real-time guidance for performing biopsies, a mpMRI-TRUS fusion has been proposed to guide targeted biopsy by combining the accuracy of mpMRI and the flexibility of TRUS [56]. The mpMRI-TRUS fusion includes a visual/cognitive way and a software-assisted way [57]. Many uncertainties such as patient position, probe position, as well as knowledge and experience of the urologists still hamper the widespread use of the fusion. As an alternative to mpMRI-TRUS fusion, in-bore MRI-targeted biopsy can be performed. However, the high cost, lengthy procedure, and difficulty in scheduling should be considered [57].

To achieve an ultrasound-only method, in the past decade, we have already developed CUDI techniques for hemodynamic quantification in the prostate by 2D and 3D DCE-US acquisitions, and have shown the efficacy of CUDI in detecting cancer angiogenesis [18,21–25,27]. Based on our previous experiences with both 2D and 3D imaging, although 2D DCE-US imaging is more widely available and today the established clinical standard, 3D DCE-US imaging can provide comprehensive

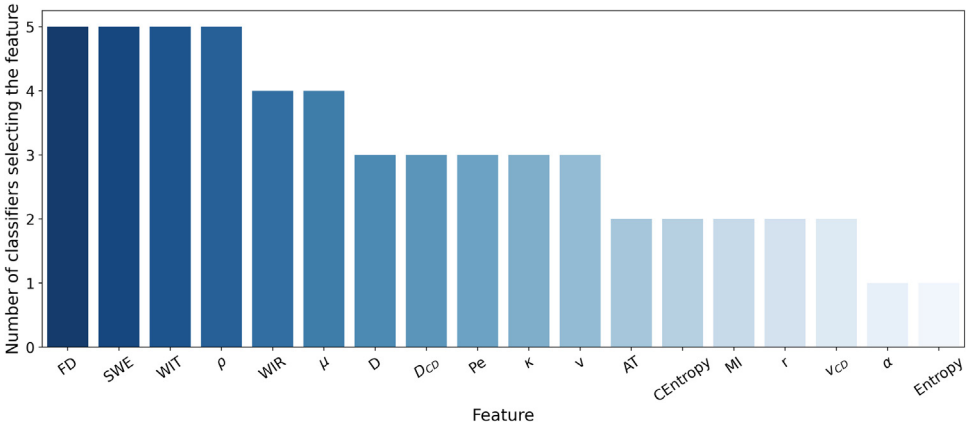

Figure 3. Multiparametric feature selection ranking plot. The number of classifiers selecting a feature (regardless of AUC) as a member of their best feature subset is expressed by the height as well as the color shade of the bar.

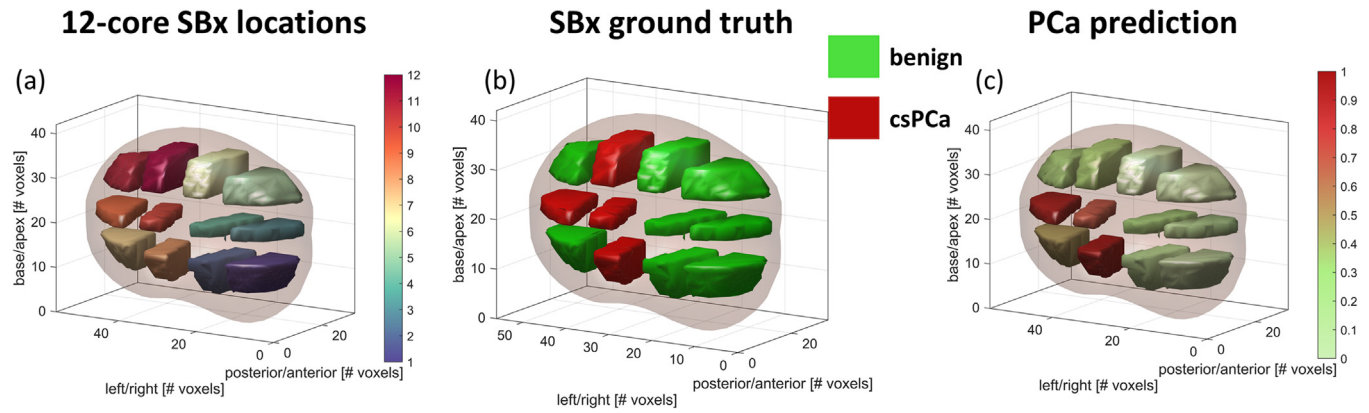

Figure 4. (a) shows the 12-core SBx regions that we segmented to compute the biopsy-region-wise radiomic features. (b) and (c) show an example of the results of the SBx ground truth and the corresponding csPCa prediction. Note that the prediction is given in terms of probability of being malignant.

information on the hemodynamics of the full prostate, describing more accurately the intrinsic behavior of blood flow and UCA perfusion; as a result, 3D imaging allows for a better definition of the boundary conditions for directly modeling the 3D behavior of UCA transport through the prostate as a convective-dispersion process. Moreover, 3D imaging enables the three-dimensional regional subdivision corresponding to SBx locations and allows for full-prostate pathology registration, which facilitates the validation of any proposed quantitative analysis. Finally, a 3D approach allows for DCE-US quantitative analysis of the full prostate by injection of a single UCA bolus, shortening the clinical workflow and facilitating its clinical translation. In this work, we considered tissue stiffness as a complementary biomarker to the tumor angiogenic biomarkers. Hence, we proposed a 3D multiparametric ultrasound imaging approach by combining CUDI-based hemodynamic quantifications and 3D ultrasound SWE-based tissue stiffness assessment to predict prostate biopsy outcomes, aiming at csPCa localization. The csPCa classification performance of the proposed approach was assessed by AUC in a group-k-fold cross-validation fashion. Moreover, the AUC value was compared to the csPCa localization performance using individual parameters and a multiparametric approach using CUDI parameters only. In general, a combination of multiple hemodynamic parameters, reflecting *e.g.,* dispersion and perfusion characteristics, is more powerful than each individual parameter for PCa diagnostics. Furthermore, the multiparametric approach combining complementary biomarkers performs better than the multiparametric approach using hemodynamic (CUDI) parameters alone. In particular, the AUC value (0.85) achieved by the multiparametric approach combining complementary biomarkers is numerically superior to the AUC value (0.78) obtained by mpMRI for csPCa detection as reported in [58].

By looking at the performance of individual parameters, it was shown that flow kinetics parameters such as velocity and dispersion obtained by 3D convective-dispersion modeling have high AUC values. This implies that tumor-driven angiogenesis is strongly associated with the local blood flow patterns [10]. The higher velocity found in tumor regions is also confirmed by the increased blood perfusion parameters, such as WIR. Moreover, the classification performance of the spatiotemporal similarities between neighboring TICs and the local dispersion parameter κ extracted from the model-fitting analysis evidence that cancer-related changes in the microvasculature architecture indeed influence the local dispersion kinetics, and further influence the shape of TICs according to the convective-dispersion process.

For each classifier, region-wise radiomic features of each parameter were used as the input. Therefore, the classifiers could select different radiomic features of the same parameter. However, in the feature selection ranking plot, we show the results only at the parameter level, regardless which and how many radiomic features derived from the same parameter were selected. The feature selection ranking plot reveals that the most frequently selected features are reflecting different tissue properties, such as the geometry of the vascular architecture (fractal dimension) and tissue stiffness, while these features do not necessarily show a good individual classification performance. This may emphasize the importance and efficacy of combining complementary biomarkers for PCa classification.

In this multiparametric approach, we implemented five classifiers as prediction model candidates and the one having the best performance was determined after feature selection and hyperparameter tuning. Compared to using one specific classifier, this strategy provides more flexibility in finding the best model. In the future, the choice of the best model would depend on the new datasets. Although five classifiers were implemented as candidates, the number of frequently selected ($\geq$3 classifiers) features is 11 out of 19. This reflects that the best feature subset remains rather insensitive to changes in the employed prediction model (classifier), underpinning the objective diagnostic value of the provided complementary ultrasound biomarkers. Moreover, the frequently selected features cover the geometrical measure of the vascular architecture (fractal dimension), tissue stiffness, wash-in perfusion parameters, TIC spatiotemporal similarities, and flow velocity and contrast dispersion, which confirm the relevance of hemodynamic quantifications and tissue stiffness for PCa diagnostics.

There are several limitations in this study. In this work, only 54 patient datasets from a single center were used to validate the proposed method. Due to the limited sample size, we did not implement nested cross-validation based on the 9 folds, in which a dedicated partition of the data is used to test the optimal model; this may lead to overfitting. Prior to feature selection, we did not remove highly correlated features based on a feature correlation matrix (*e.g.,* the linear Pearson correlation coefficient). Despite this, the classifiers have selected complementary parameters as shown in the feature selection ranking plot. Furthermore, the proposed method is based on biopsy regions by subdividing each 3D prostate into 12 regions according to the SBx template shown by Ukimura *et al.* [48]. However, the biopsy track is difficult to evaluate; therefore, the actual SBx locations may mismatch the template, which to some extent influences the accuracy of the adopted ground truth. Moreover, biopsies may intrinsically miss cancer regions, leading to underdiagnosis and an overestimated number of false positives by the proposed approach.

To solve these limitations, we have recently started a multicenter trial to build a larger patient cohort [59]. Firstly, including more patients allows for further validation of the results and optimization of the machine-learning procedure using nested cross-validation. In this trial, we are collecting full-prostate pathology samples after radical prostatectomy, and are performing DCE-US and SWE scans using the same probe and the same scanner, facilitating the clinical workflow and reducing possible registration errors. As such, a voxel-level

multiparametric approach by correlating the 3D CUDI parameters and SWE elasticity to the full-prostate pathology model can be investigated. This will alleviate the limitation of biopsies missing cancer regions. Moreover, more ultrasound biomarkers can be added as feature candidates in the multiparametric ultrasound approach; for instance, tissue texture features extracted from ultrasound B-mode images and DCE-US recordings [60–62], blood flow velocity obtained from ultrasound power Doppler image [63,64], and microvasculature structural information provided by DCE-US tractography [65]. These can all be integrated in the proposed multiparametric approach and evaluated for their contribution to PCa detection. From a technical point of view, these measures may further improve the performance of the proposed multiparametric approach and enhance the reliability of the trained classification model. From a clinical point of view, given that this new clinical trial will exclusively involve patients referred for radical prostatectomy, there is a susceptibility to selection bias. Consequently, the diagnostic performance observed in this study may not be generalizable to the broader population. This bias can be mitigated by adjusting the voxel prevalence in the training set of the classifier. Yet, to establish the definitive efficacy of 3D multiparametric ultrasound imaging for PCa diagnosis in biopsy naïve patients, a further prospective study of image-based biopsy targeting is also planned. Along with the new clinical trial, the feasibility of embedding multiparametric ultrasound imaging in the clinical workflow, enabling PCa prediction and localization immediately after acquiring all the data, is being investigated. As CUDI analysis is one of the current bottlenecks, solutions for fast execution are currently being pursued. Once the CUDI parameters are obtained, other ultrasound features together with the CUDI parameters will be input into a trained classification model to localize PCa and predict its aggressiveness, providing urologists with a reference for *e.g.,* targeting biopsies.

Conclusions

In conclusion, the proposed biopsy-region-based multiparametric ultrasound imaging approach yields promising results for the prediction of biopsy outcome, enabling csPCa localization, which underlines the importance of combining complementary ultrasound biomarkers for cancer detection. These results also establish a basis for further developments towards prostate biopsy targeting by a multiparametric ultrasound approach. We believe that our ongoing multicenter trial will further support these results and improve the performance of the proposed method.

Data availability statement

The research data are confidential due to ethical restrictions.

Acknowledgments

This work is supported by the research program LOCATE with project number 15282, which is financed by the Dutch Research Council (NWO-TTW).

Conflict of interest

Prof. Massimo Mischi and Prof. Hessel Wijkstra are the advisors of the company Angiogenesis Analytics (the Netherlands).

References

[1] Siegel RL, Miller KD, Fuchs HE, Jemal A. Cancer statistics, 2022. CA Cancer J Clin 2022;72(1):7–33.
[2] Barentsz JO, Richenberg J, Clements R, Choyke P, Verma S, Villeirs G, et al. ESUR prostate MR guidelines 2012. Eur Radiol 2012;22:746–57.
[3] Mottet N, van den Bergh RCN, Briers E, Van den Broeck T, Cumberbatch MG, De Santis M, et al. EAU-EANM-ESTRO-ESUR-SIOG Guidelines on Prostate Cancer-2020 Update. Part 1: screening, diagnosis, and local treatment with curative intent. Eur Urol 2021;79(2):243–62.
[4] Schoots IG, Roobol MJ, Nieboer D, Bangma CH, Steyerberg EW, Hunink MGM. Magnetic resonance imaging–targeted biopsy may enhance the diagnostic accuracy of significant prostate cancer detection compared to standard transrectal ultrasound-guided biopsy: a systematic review and meta-analysis. Eur Urol 2015;68(3):438–50.
[5] Carlsson S, Benfante N, Alvim R, Sjoberg DD, Vickers A, Reuter VE, et al. Long-term outcomes of active surveillance for prostate cancer: the Memorial Sloan Kettering Cancer center experience. J Urol 2020;203(6):1122–7.
[6] Ahmed HU, El-Shater Bosaily A, Brown LC, Gabe R, Kaplan R, Parmar MK, et al. Diagnostic accuracy of multi-parametric MRI and TRUS biopsy in prostate cancer (PROMIS): a paired validating confirmatory study. Lancet 2017;389 (10071):815–22.
[7] Loch T. Prostate cancer diagnostics: innovative imaging in case of multiple negative biopsies. World J Urol 2011;29(5):607–14.
[8] Mottet N, Cornford P, van den Bergh RCN, Briers E, Expert Patient Advocate, De Santis M, et al. EAU-EANM-ESTRO-ESUR-ISUP_SIOG-Guidelines-on-Prostate-Cancer-2022. EAU Guidelines. Edn. presented at the EAU Annual Congress Amsterdam 2022. ISBN 978-94-92671-16-5. EAU Guidelines Office, Arnhem, The Netherlands. 2022.
[9] Smeenge M, De La Rosette JJMCH, Wijkstra H. Current status of transrectal ultrasound techniques in prostate cancer. Curr Opin Urol 2012;22(4):297–302.
[10] Folkman J. Role of angiogenesis in tumor growth and metastasis. Semin Oncol 2002;29(6 Suppl 16):15–8.
[11] Russo G, Mischi M, Scheepens W, la Rosette JJD, Wijkstra H. Angiogenesis in prostate cancer: onset, progression and imaging. BJU Int 2012;110(11c):E794–808.
[12] Tang J, Yang JC, Luo Y, Li J, Li Y, Shi H. Enhancement characteristics of benign and malignant focal peripheral nodules in the peripheral zone of the prostate gland studied using contrast-enhanced transrectal ultrasound. Clin Radiol 2008;63(10):1086–91.
[13] Elie N, Kaliski A, Péronneau P, Opolon P, Roche A, Lassau N. Methodology for quantifying interactions between perfusion evaluated by DCE-US and hypoxia throughout tumor growth. Ultrasound Med Biol 2007;33(4):549–60.
[14] Postema AW, Frinking PJA, Smeenge M, De Reijke TM, De La Rosette JJMCH, Tranquart F, et al. Dynamic contrast-enhanced ultrasound parametric imaging for the detection of prostate cancer. BJU Int 2016;117(4):598–603.
[15] Eckersley RJ, Michiel Sedelaar JP, Blomley MJK, Wijkstra H, Desouza NM, Cosgrove DO, et al. Quantitative microbubble enhanced transrectal ultrasound as a tool for monitoring hormonal treatment of prostate carcinoma. Prostate 2002;51(4):256–67.
[16] Rognin NG, Frinking P, Costa M, Arditi M. In-vivo perfusion quantification by contrast ultrasound: Validation of the use of linearized video data vs. raw RF data. In: Proceedings - IEEE Ultrasonics Symposium; 2008. p. 1690–3.
[17] Mischi M, Kalker T, Korsten E. Videodensitometric methods for cardiac output measurements. EURASIP J Appl Signal Processing 2003;2003(5):479–89.
[18] Kuenen MPJ, Mischi M, Wijkstra H. Contrast-ultrasound diffusion imaging for localization of prostate cancer. IEEE Trans Med Imaging 2011;30(8):1493–502.
[19] Kuenen MPJ, Saidov TA, Wijkstra H, De La Rosette JJMCH, Mischi M. Spatiotemporal correlation of ultrasound contrast agent dilution curves for angiogenesis localization by dispersion imaging. IEEE Trans Ultrason Ferroelectr Freq Control 2013;60 (12):2665–9.
[20] Kuenen MPJ, Saidov TA, Wijkstra H, Mischi M. Contrast-ultrasound dispersion imaging for prostate cancer localization by improved spatiotemporal similarity analysis. Ultrasound Med Biol 2013;39(9):1631–41.
[21] Mischi M, Kuenen MPJ, Wijkstra H. Angiogenesis imaging by spatiotemporal analysis of ultrasound contrast agent dispersion kinetics. IEEE Trans Ultrason Ferroelectr Freq Control 2012;59(4):621–9.
[22] van Sloun RJ, Demi L, Postema AW, de la Rosette JJ, Wijkstra H, Mischi M. Ultrasound-contrast-agent dispersion and velocity imaging for prostate cancer localization. Med Image Anal. 2017;35:610–9.
[23] Wildeboer RR, Postema AW, Demi L, Kuenen MPJ, Wijkstra H, Mischi M. Multiparametric dynamic contrast-enhanced ultrasound imaging of prostate cancer. Eur Radiol 2017;27(8):3226–34.
[24] Wildeboer RR, Mannaerts CK, van Sloun RJG, Budäus L, Tilki D, Wijkstra H, et al. Automated multiparametric localization of prostate cancer based on B-mode, shear-wave elastography, and contrast-enhanced ultrasound radiomics. Eur Radiol 2020;30(2):806–15.
[25] Wildeboer RR, van Sloun RJG, Huang P, Wijkstra H, Mischi M. 3-D multi-parametric contrast-enhanced ultrasound for the prediction of prostate cancer. Ultrasound Med Biol 2019;45(10):2713–24.
[26] Schalk SG, Demi L, Smeenge M, Mills DM, Wallace KD, De La Rosette JJMCH, et al. 4-D spatiotemporal analysis of ultrasound contrast agent dispersion for prostate cancer localization: a feasibility study. IEEE Trans Ultrason Ferroelectr Freq Control 2015;62(5):839–51.
[27] Wildeboer RR, Van Sloun RJG, Schalk SG, Mannaerts CK, Van Der Linden JC, Huang P, et al. Convective-dispersion modeling in 3D contrast-ultrasound imaging for the localization of prostate cancer. IEEE Trans Med Imaging 2018;37 (12):2593–602.
[28] Wildeboer RR, Van Sloun RJG, Mannaerts CK, Van der Linden JC, Huang P, Wijkstra H, et al. Probabilistic 3D Contrast-ultrasound tractography based on aa convective-dispersion finite-element scheme: 2018. IEEE International Ultrasonics Symposium (IUS); 2018.
[29] Pallwein L, Mitterberger M, Gradl J, Aigner F, Horninger W, Strasser H, et al. Value of contrast-enhanced ultrasound and elastography in imaging of prostate cancer. Curr Opin Urol 2007;17(1):39–47.

[30] Hoyt K, Castaneda B, Zhang M, Nigwekar P, di Sant'Agnese PA, Joseph J V, et al. Tissue elasticity properties as biomarkers for prostate cancer. Cancer Biomark 2008;4(4–5):213–25.
[31] Correas JM, Tissier AM, Khairoune A, Vassiliu V, Méjean A, Hélénon O, et al. Prostate cancer: diagnostic performance of real-time shear-wave elastography. Radiology 2015;275(1):280–9.
[32] Boehm K, Salomon G, Beyer B, Schiffmann J, Simonis K, Graefen M, et al. Shear wave elastography for localization of prostate cancer lesions and assessment of elasticity thresholds: implications for targeted biopsies and active surveillance protocols. J Urol 2015;193(3):794–800.
[33] Woo S, Suh CH, Kim SY, Cho JY, Kim SH. Shear-wave elastography for detection of prostate cancer: a systematic review and diagnostic meta-analysis. AJR Am J Roentgenol 2017;209(4):806–14.
[34] Sang L, Wang XM, Xu DY, Cai YF. Accuracy of shear wave elastography for the diagnosis of prostate cancer: a meta-analysis. Sci Rep 2017;7(1):1949.
[35] Shoji S, Hashimoto A, Nakamura T, Hiraiwa S, Sato H, Sato Y, et al. Novel application of three-dimensional shear wave elastography in the detection of clinically significant prostate cancer. Biomed Rep 2018;8(4):373–7.
[36] Postema A, Mischi M, de la Rosette J, Wijkstra H. Multiparametric ultrasound in the detection of prostate cancer: a systematic review. World J Urol 2015;33(11):1651–9.
[37] Jung N, DiNatale RG, Frankel J, Koenig H, Ho O, Flores JP, et al. The role of multiparametric ultrasound in the detection of clinically significant prostate cancer. World J Urol 2023;41(3):663–71.
[38] Grey ADR, Scott R, Shah B, Acher P, Liyanage S, Pavlou M, et al. Multiparametric ultrasound versus multiparametric MRI to diagnose prostate cancer (CADMUS): a prospective, multicentre, paired-cohort, confirmatory study. Lancet Oncol 2022;23(3):428–38.
[39] Morris DC, Chan DY, Lye TH, Chen H, Palmeri ML, Polascik TJ, et al. Multiparametric ultrasound for targeting prostate cancer: combining ARFI, SWEI, QUS and B-mode. Ultrasound Med Biol 2020;46(12):3426–39.
[40] Demené C, Deffieux T, Pernot M, Osmanski BF, Biran V, Gennisson JL, et al. Spatiotemporal clutter filtering of ultrafast ultrasound data highly increases Doppler and fultrasound sensitivity. IEEE Trans Med Imaging 2015;34(11):2271–85.
[41] Taylor G. Dispersion of soluble matter in solvent flowing slowly through a tube. Proc R Soc London Ser A Math Phys Sci 1953;219(1137):186–203.
[42] Norwich KH, Zelin S. The dispersion of indicator in the cardio-pulmonary system. Bull Math Biophys 1970;32(1):25–43.
[43] Marbach S, Alim K. Active control of dispersion within a channel with flow and pulsating walls. Phys Rev Fluids 2019;4(11):114202.
[44] van Brakel J, Heertjes PM. Analysis of diffusion in macroporous media in terms of a porosity, a tortuosity and a constrictivity factor. Int J Heat Mass Transf 1974;17(9):1093–103.
[45] Schalk SG, Demi L, Bouhouch N, Kuenen MPJ, Postema AW, De La Rosette JJMCH, et al. Contrast-enhanced ultrasound angiogenesis imaging by mutual information analysis for prostate cancer localization. IEEE Trans Biomed Eng 2017;64(3):661–70.
[46] Van Sloun RJ, Demi L, Postema AW, Jmch De La Rosette J, Wijkstra H, Mischi M. Entropy of ultrasound-contrast-agent velocity fields for angiogenesis imaging in prostate cancer. IEEE Trans Med Imaging 2017;36(3):826–37.
[47] Saidov T, Heneweer C, Kuenen M, von Broich-Oppert J, Wijkstra H, de la Rosette J, et al. Fractal dimension of tumor microvasculature by DCE-US: preliminary study in mice. Ultrasound Med Biol 2016;42(12):2852–63.
[48] Ukimura O, Coleman JA, De La Taille A, Emberton M, Epstein JI, Freedland SJ, et al. Contemporary role of systematic prostate biopsies: indications, techniques, and implications for patient care. Eur Urol 2013;63(2):214–30.
[49] Gillies RJ, Kinahan PE, Hricak H. Radiomics: images are more than pictures, they are data. Radiology 2016;278(2):563–77.
[50] Pudil P, Novovičová J, Kittler J. Floating search methods in feature selection. Pattern Recognit Lett 1994;15(11):1119–25.
[51] Akiba T, Sano S, Yanase T, Ohta T, Koyama M. Optuna: a next-generation hyperparameter optimization framework. Proc 25th ACM SIGKDD Int Conf Knowl Discov Data Min.
[52] Shapiro SS, Wilk MB. An analysis of variance test for normality (complete samples). Biometrika 1965;52(3–4):591–611.
[53] Bott SRJ, Ahmed HU, Hindley RG, Abdul-Rahman A, Freeman A, Emberton M. The index lesion and focal therapy: an analysis of the pathological characteristics of prostate cancer. BJU Int 2010;106(11):1607–11.
[54] Wise AM, Stamey TA, McNeal JE, Clayton JL. Morphologic and clinical significance of multifocal prostate cancers in radical prostatectomy specimens. Urology 2002;60(2):264–9.
[55] Villers A, Mcneal JE, Freiha FS, Stamey TA. Multiple Cancers in the prostate morphologic features of clinically recognized versus incidental tumors.
[56] Zhang F, Zhang S, Huang H, Zhang Q, Zhang S, Zhang S, et al. Analysis of the cause of missed diagnosis in mpMRI/TRUS fusion-guided targeted prostate biopsy. BMC Urol 2022;22(1):1–5.
[57] Venderink W, Bomers JG, Overduin CG, Padhani AR, de Lauw GR, Sedelaar MJ, et al. Multiparametric magnetic resonance imaging for the detection of clinically significant prostate cancer: what urologists need to know. Part 3: Targeted Biopsy. Eur Urol 2020;77(4):481–90.
[58] Xu L, Zhang G, Shi B, Liu Y, Zou T, Yan W, et al. Comparison of biparametric and multiparametric MRI in the diagnosis of prostate cancer. Cancer Imaging 2019;19(1):1–8.
[59] Jager A, Postema AW, Mischi M, Wijkstra H, Beerlage HP, Oddens JR. Clinical trial protocol: developing an image classification algorithm for prostate cancer diagnosis on three-dimensional multiparametric transrectal ultrasound. Eur Urol Open Sci 2023;49:32–43.
[60] Han SM, Lee HJ, Choi JY. Computer-aided prostate cancer detection using texture features and clinical features in ultrasound image. J Digit Imaging 2008;21(SUPPL. 1):121–33.
[61] Mohamed SS, Salama MMA, Kamel M, El-Saadany EF, Rizkalla K, Chin J. Prostate cancer multi-feature analysis using trans-rectal ultrasound images. Phys Med Biol 2005;50(15):N175.
[62] Theek B, Opacic T, Magnuska Z, Lammers T, Kiessling F. Radiomic analysis of contrast-enhanced ultrasound data. Sci Reports 2018;8(1):1–9.
[63] Kahraman T, Cubuk R, Sinanoglu O, Tasalı N, Ozarar M, Saydam B. Comparison of power doppler ultrasound with gray scale transrectal ultrasound in predicting cancer positive prostate biopsy cores. Eurasian J Med 2010;42(2):81.
[64] Inahara M, Suzuki H, Nakamachi H, Kamiya N, Shimbo M, Komiya A, et al. Clinical evaluation of transrectal power Doppler imaging in the detection of prostate cancer. Int Urol Nephrol 2004;36(2):175–80.
[65] van Sloun RJG, Demi L, Schalk SG, Caresio C, Mannaerts C, Postema AW, et al. Contrast-enhanced ultrasound tractography for 3D vascular imaging of the prostate. Sci Rep 2018;8(1):1–8.